Shattering impact fragmentation of slender nanoprojectiles

S Mastilovic*

Institute for Multidisciplinary Research, University of Belgrade, Kneza Viseslava 1, 11030 Belgrade, Serbia

Abstract

Molecular dynamics simulations of the rigid-anvil collision test are performed to achieve the complete pulverization of slender nanoprojectiles. The simulation setup mimics the traditional Taylor test (the flat-ended nanoscale bars collide with a rough rigid wall) at striking velocities that reach an awesome range from 20 km/s to 120 km/s. The objective is to investigate, so called, shattering fragmentation, defined by the complete disintegration (pulverization) of the slender monocrystalline nanoprojectile into the cloud of monatomic debris ($m_{max} = m_{max1} \equiv 1$). The critical impact energy associated with this transition from the stochastic to the deterministic fragment distribution is investigated at two widely different initial temperatures of the slender nanoprojectile while scaling its size in a self-similar manner by varying their widths (diameters) at a fixed aspect ratio. For all but the smallest nanoprojectiles, the minimum achievable $m_{max} >> m_{max1}$ is discussed based on the physically-limiting striking velocity range.

Keywords

Taylor test · Impact fragmentation · Shattering fragmentation · Hypervelocity impact

1 Introduction

Fragmentation is an irreversible kinetic phenomenon that occurs in numerous processes that cover a vast range of spatial and temporal scales. The ultrafast collision of the flat-ended projectile with the rigid target [1] is an extremely intense loading event belonging to the realm of akrology within the study of materials' physics. The extremely steep gradients of state variables (e.g., [2]), well documented by shock experiments [3, 4], may cause phase transitions and lead to sequential fractures that culminate eventually in energetic expulsion of fragment debris. Since the shock wave excitation is inherently ultrafast, the present molecular dynamics (MD) method requires a sub-femtosecond time resolution to observe the collective dynamics of material on picosecond time scales and to reach the shattering transition, which renders simulations time-consuming.

The fundamental principles of dynamic fragmentation of solids were investigated extensively in the past—theoretically, experimentally and numerically—and the substantial literature is compiled recently [5, 6, 7]. Examples of computational techniques utilized in the last decade in the dynamic fracture and fragmentation investigations include: MD [8-10]; particle models [11-13], lattice and discrete element models [14-19], finite element methods [20-22], and meshfree methods [23-25].

The shattering transition [26] is identified herein with a change from the stochastic fragment phase to the deterministic dust phase corresponding to the uniformly monatomic debris ($m_{max} \equiv 1$). (Note that hereinafter the fragment mass m and the nanoprojectile mass M are presented in units of m_0; i.e., the number of atoms composing them.) The term "shattering" is inspired by Redner's discussion of a mathematical pathology in a solution of the linear fragmentation rate equation (identified by the singularity of the kinetic exponent) "in which mass is lost to a dust phase consisting of an infinite number of zero mass particles" [27]. Needless to say, not only the critical point

*Corresponding author:
Email: misko.mastilovic@imsi.bg.ac.rs, Tel: +381 64 2360-444

coordinates, i.e. (v_1, $m_{max} \equiv 1$), but also the mere achievability of this transition, are strongly dependent on the system size. In the following investigation, this system size is, for an arbitrarily fixed aspect ratio (length/width = $L/d \approx 7.1 \div 7.3$; Fig. 1a), reflected by the width (diameter) of the slender nanoprojectile, $\bar{d} = d/r_0$ [1]. This elusive terminal fragmentation, predicted by the piecewise-linear model [10] to correspond to the impact velocity of approximately 45 km/s, has not been achieved in earlier investigations even at much higher striking velocities [28]. The capturing of the shattering fragmentation in the above-described manner may appear a purely academic endeavor. Be it as it may, it is a final ingredient necessary to complete the emerging reverse-sigmoid phenomenological model aimed at encapsulating unifying features of the nonlinear and saturable dependence of the maximum fragment mass upon the set of impact parameters and ballistic state variables.

With this goal in mind, the series of 2D-MD simulations of the ballistic Taylor test [1] is augmented in this study by introducing: (i) an additional interatomic potential, (ii) the Nose-Hoover thermostat [29] fixing the initial (pre-impact) temperature, (iii) attosecond time steps, and (iv) increased-atomic density targets addressing the problem of embedding the projectile atoms into the target lattice at enormous striking powers. Thus, the slender, flat-ended nanoprojectiles are made of a monocrystalline solid modelled either by the Lennard-Jones 6-12 (LJ) potential or the embedded-atom method (EAM) with a tacit assumption that the simplicity of these generic models does not impede the qualitative investigation aiming at general trends of nanoscale fragmentation.

2 Computer simulation technique

The present investigation is based on the traditional MD in which the dynamic state of an atomic system is defined by laws of classical mechanics with atomic motions being uniquely determined by an empirical potential. A monatomic system is comprised of atoms of equal masses (m_0) that form an ideal defect-free triangular lattice (without any quenched disorder) and interact with their nearest neighbors according to either the LJ potential or the EAM to mimic a monocrystalline, flat-nosed nanoprojectile (Figs. 1a and 2). The former rudimentary model—expressed by Eq. (1b)—is described in detail in preceding studies [2, 10, 28], thus, a succinct summary is deemed sufficient herein.

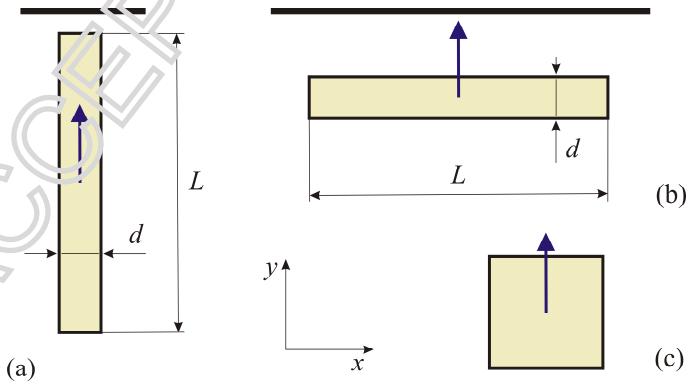

Fig. 1. Schematics of the rigid-anvil impact simulations: (a) the *basic* model – the traditional Taylor test (TTT), (b) the lateral (side) impact test (LIT), and (c) the square-projectile impact (approximately the same mass as the preceding two). The latter two configurations are used solely for the investigation of the structural sensitivity of results (Section 3.2). The blue arrows depict the striking velocity direction. (The aspect ratio of the projectile in the first two setups and the masses of all three projectiles are as close as the 2D lattice discretization allows.)

[1] Rigorously, since the present two-dimensional (2D) model is not written in cylindrical/axisymmetric coordinates, d is simply a width (lateral dimension), instead of a diameter of the nanoprojectile (implying a circular cross-section). Nonetheless, the term diameter is occasionally retained hereinafter for the sake of clarity and to emphasize the analogy with three-dimensional Taylor test.

The model parameters are selected based on the following physical properties of tungsten ($_{74}$W): the atomic mass $m_0 = 3.1\times10^{-25}$ kg (183.85 u), the atomic radius 1.4 Å ($\equiv r_0/2$, where r_0 is the equilibrium interatomic distance), and the strength of attraction $\varepsilon = 7.5\times10^{-20}$ J [2]. The initial projectile size (14.5×104 nm corresponding to $\bar{d} = 53$) is scaled as indicated throughout the investigation to pursue the stated objective, but the aspect ratio (L/d) is kept constant. The coordination number of bulk atoms in all reference configuration is six and the potential energy per atom is—depending on the system size—slightly in excess of the bulk value (–3 ε) due to the surface effects. (These effects make the impact-fragmentation results size dependent, which is well known and explored; e.g., [30].) Prior to collision, the projectile made of LJ solid is prepared at zero temperature while the EAM projectile is prepared either at 1 K or 1000 K (Fig. 2). The latter is selected arbitrarily, below the melting temperature of tungsten, to explore the effect of the elevated initial temperature.

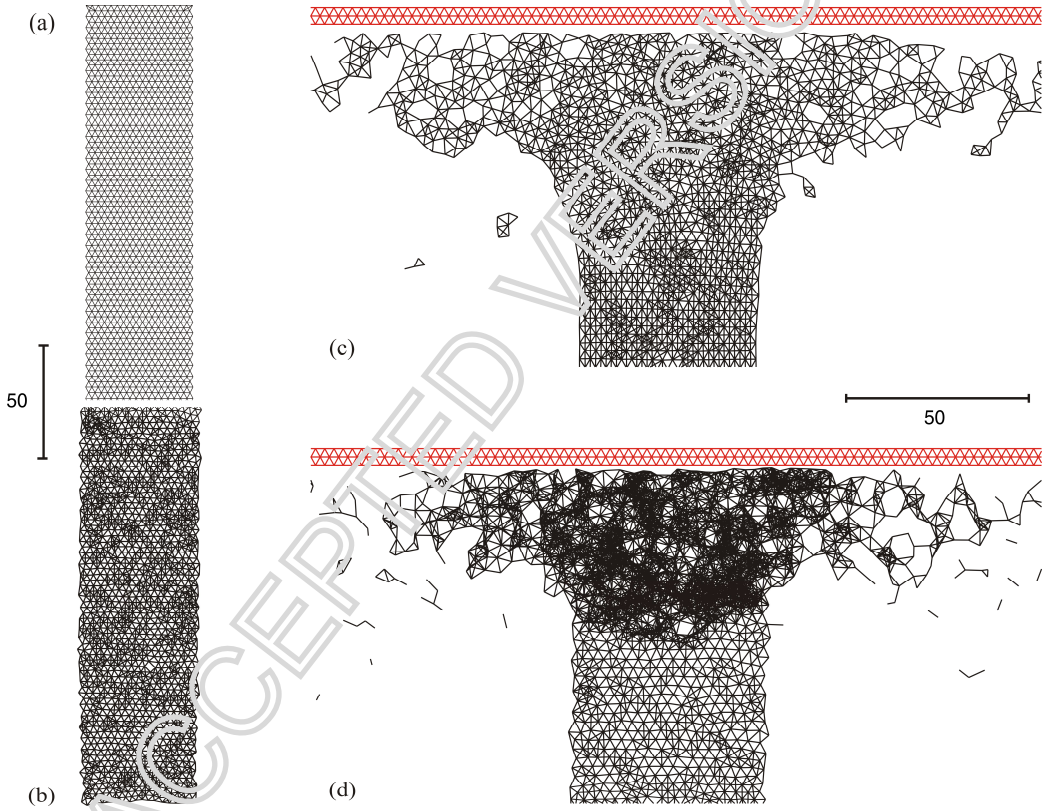

Fig. 2. Details of initial and deformed configurations of EAM nanoprojectiles with $\bar{d} = 18$. Figures (a) and (b) represent proximal and distal halves of nanoprojectiles (relative to the target; Fig. 1a) equilibrated at $T_0 = 1$ K and $T_0 = 1000$ K, respectively. Both deformed configurations refer to the systems initially equilibrated at 1000 K, but with two widely different striking velocities: (c) $v = 1$ km/s ($t = 0.1$ ps, $\Delta t = 2.5$ fs), and (d) $v = 98$ km/s ($t = 0.015$ ps, $\Delta t = 0.025$ fs). The increase of density of interatomic bonds in (d) compared to (c) reflects the enormous surge of pressure in the contact zone inherent to the extreme-hypervelocity impacts. (The lengths markers are presented in Å.)

The EAM is constructed by following the time-honored approach of Holian and co-authors [31]. In short, the total configuration energy

$$\Phi = \sum_{i=1}^{N}\left[\frac{1}{2}\chi\sum_{j\neq i}\varphi(r_{ij}) + (1-\chi)\,\Im(\rho_i)\right] \tag{1a}$$

is the sum of:

- the pairwise-additive contribution,

$$\varphi = \varphi(r_{ij}) = -\varepsilon\left[2\,(r/r_0)_{ij}^{-6} - (r/r_0)_{ij}^{-12}\right] \tag{1b}$$

that has of the same density-independent form and parameters as the preceding LJ model, and

- the embedding energy,

$$\Im = \Im(\rho_i) = E_{coh}\,(\rho/\rho_0)_i \ln \rho_i \tag{1c}$$

that depends on the local environmental density (of electrons provided by the remaining atoms of the system). In the EAM of Holian and co-authors [31], this atomic electron density is defined by a pairwise sum over all neighboring atoms, $\rho_i = \sum w\,(r_{ij})$, weighted by a spherical localization function

$$w(r_{ij}) = w_0\left(\frac{r_{\max}^2 - r_{ij}^2}{r_{\max}^2 - r_0^2}\right)^2, \quad w_0 = w(r_0) = \frac{\varepsilon}{E_{coh}} \frac{\rho_0}{2} \tag{1d}$$

In the preceding expressions, $\chi \approx 1/3$ is the fractional pair-potential contribution to the total cohesion, $E_{coh} = D(D+1)\varepsilon/2$ is the cohesive energy of the D-dimensional system, ρ_0 is the normal local density (evaluated at the equilibrium configuration and corresponding, in this case, to the reciprocal value of the base of the natural logarithm), $r_{\max}$ is the potential cutoff distance, and lowercase subscripts i and j indicate atom labels [31]. The sensitivity of the simulation results to the Holian and co-authors' choice of $\chi \approx 1/3$ [31] is explored, and it is concluded that the selected value is acceptable for the present study. The particularly appealing aspect of the EAM is its physical picture of metallic bonding [32].

As mentioned before, the EAM system is, in the present study, initially equilibrated at two widely-different arbitrarily-selected temperatures (T_0 = 1 K and 1000 K) by using the Nose-Hoover thermostat [29]. During the initial thermal equilibration, the equations of Nose-Hoover dynamics are solved numerically by using the Størmer algorithm

$$r(t) = r(t - \Delta t) + \dot{r}(t - \Delta t/2)\,\Delta t + \mathrm{O}(\Delta t^3) \tag{2a}$$

$$\zeta(t) = \zeta(t - \Delta t) + \upsilon\left[\frac{T(t - \Delta t/2)}{T_0} - 1\right]\Delta t + \mathrm{O}(\Delta t^3) \tag{2b}$$

$$\dot{r}(t + \Delta t/2) = \frac{1}{1 + \upsilon\,\zeta(t)\,\Delta t/2}\left\{\dot{r}(t - \Delta t/2)\left[1 - \upsilon\,\zeta(t)\,\Delta t/2\right] + \ddot{r}(t)\,\Delta t\right\} + \mathrm{O}(\Delta t^3) \tag{2c}$$

(The vector notation and particle indices are dropped for brevity.) Since the shock wave excitation is inherently ultrafast, the Cauchy problem is solved with the time step Δt of the order of fraction of femtoseconds (Table 1). The physical basis for the *initial* timestep estimate, that insures MD simulation stability, is discussed in [2]. Depending on the striking velocity and projectile size (i.e., the impact energy), this timestep is further reduced to supress the embedding of the projectile atoms into the surface layers of the rigid target (Table 1). Regardless of this *timestep reduction*, for the highest striking velocities and the largest nanoprojectiles used in the present study, it is not possible to prevent the occasional embedding. In order to address this problem, the atomic density of the target is increased by reduction of the interatomic density, as discussed shortly. The extremely small time resolution (e.g., [33]), required by the *ultrahigh power density* of the simulated event, in conjunction with necessity to reach the shattering fragmentation, makes the MD simulations time-consuming even for the inherently small (as it will be observed later) model size, and effectively limits the maximum achievable striking velocity.

In the reversible central-difference equations (2), υ is the rate of coupling of the thermostat to the atoms, and ζ is the dimensionless flow variable defined by $\dot{\zeta} = \upsilon\left[T/T_0 - 1\right]$ [29]. In the present study,

the initial value of υ of the order of terahertz is estimated based on deliberations in the source reference [29] and the model parameters selected herein. This value is then varied for almost two orders of magnitude until $\upsilon = 45$ THz is adopted based on the time history of the initial temperature during thermal equilibration. This huge value is intrinsically related to the selection of the time step discussed above. The thermostat is, naturally, turned off (i.e., $\upsilon = 0$) at the moment of collision to capture the temperature surge immanent to the shock loading. Thus, the purpose of the thermostat is to provide the initial configuration of the Newtonian system (atomic positions and the corresponding velocity field) for the impact simulation.

The sizes of nanoprojectile $\bar{d} \in \{19, 33, 45, 53, 57, 65\}$, used in the preceding study [30] to simulate the traditional Taylor test and study the size effect, are scaled in the present investigation to include $\bar{d} \in \{5, 7, 9, 11, 13, 15, 17, 18, 19, 21, 22, 23\}$. As mentioned above, in order to suppress occasional embedding of the projectile atoms into the target lattice at the highest impact energy densities, that may contaminate the investigation results, some simulations are—as indicated in Table 1—performed with an increased interatomic density of the rigid target achieved by the reduction of the interatomic distance $(\bar{r}_{0\mathrm{T}} = r_{0\mathrm{T}} / r_0 = 0.9)$. The sensitivity of simulation results to this change of target interatomic distance—same as the projectile $(\bar{r}_{0\mathrm{T}} = 1)$ and the increased $(\bar{r}_{0\mathrm{T}} = 0.9)$—is explored for $\bar{d} = 15$ as depicted in Fig. 5. Finally, the target density had to be further increased $(\bar{r}_{0\mathrm{T}} = 0.85)$ for the two largest projectiles used in this study ($\bar{d} = 22, 23$). The sensitivity of simulation results to this $\bar{r}_{0\mathrm{T}}$ reduction—from 0.9 to 0.85—is explored for $\bar{d} = 19$ as indicated in Fig. 5. Thus, the targets of increased atomic density are necessitated by the specific investigation objective and treated as an additional input variable in the present study.

The various combinations of two interatomic potentials (LJ and EAM) and three initial temperatures (0 K, 1 K, 1000 K) are randomly assigned to the new set of nanoprojectile sizes (as indicated in Table 1 and Fig. 5) to explore their effect on the simulation results. This random, arbitrary assignment is driven by two objectives: (i) to evenly spread the above-mentioned simulation parameters within the explored $\bar{d}$ range, and (ii) to improve the clarity of the results presented Fig. 5 (by reducing the overlap of symbols).

Table 1. The simulation plan. The corresponding results are presented in Fig. 5. (Time steps are given in attoseconds [1 as = 1×10^{-18} s].[2])

$\bar{d}$ [–]	5	7	9	11		13	15	17	18	19	21	22	23
Int. Pot.	LJ	LJ	EAM	LJ	LJ	EAM	EAM	LJ	EAM	EAM	LJ	EAM	EAM	LJ
T_0 [K]	0	0	1	0	0	1000	1	0	1	1000	0	1	1000	0
Δt [as]	50	50	50	50	50	25	25	50	25	25	25	25	25	25
$\bar{r}_{0\mathrm{T}}$ [–]	1	1	1,0.9	1	1	0.9	0.9	1	0.9	0.9	0.9	0.9	0.85	0.85

Additionally, in order to explore the structural sensitiveness of results, simulations are also performed in the lateral impact setup (Fig. 1b), with slender nanoprojectiles corresponding to a subset $\bar{d} \in \{9, 13, 17\}$ being laid perpendicular to the impact direction. Note that, due to the triangular atomic initial configuration (e.g., Fig. 2a), the slender nanoprojectiles belonging to the latter subset upon the

[2] Time steps of this size are not unheard of in the contemporary MD. Attosecond science is a novel research area in which advanced MD calculations are performed at the time resolution of a few attoseconds whenever occurrence of some salient physical events necessitates such fine time scales (e.g., [33]).

90°-rotation[3] (performed to assume the lateral impact configuration), transform, within the current MD framework, to the corresponding projectile lattices, 61×11, 89×15, and 119×19, respectively, to retain, as close as possible, the same mass and aspect ratio of the original projectiles.

The link between two atoms ruptures when their mutual distance exceeds a predetermined critical value. This cut-off interatomic distance, $R \approx 1.7\, r_0$, is selected herein to be between the first and second nearest neighbors in the reference triangular configuration of the perfect crystal prior to the thermal equilibration (note that $R = r_{max}$ of Eq. (1d)). A fragment is defined as a self-bound cluster of atoms with interatomic distance less than the cut-off distance ($r \le R$) in a sequential atom-by-atom search for the nearest neighbors [2, 10]. Importantly, the shattering fragmentation is beset with aleatory variability; with monotonic increase of the striking velocity (for the fixed nanoprojectile size), the shattering fragmentation after the initial appearance, may disappear, and reappear. The shattering transition onsets reported in the present study refer to the *first* appearance of $n_{max} = 1$ in the stationary fragment distribution for the system size in question.

It cannot be overemphasized that the fragmentation models proposed herein are generic in the sense that they aim to capture a specific feature of the investigated phenomenon on the given spatial and temporal scales. Their simplicity rests primarily on the 2D geometry and the elementary potentials. On the other hand, it will become obvious from the simulation results that the nanoscale projectile size *is not* a simplification but rather a *necessary condition* to achieve the shattering fragmentation. It has been already emphasized that the MD fragmentation simulation is a slow process, difficult to reach stationary fragment distribution [10, 34, 45]. Therefore, although the dimensionality of the system is known to influence shock physics and the universality classes of fragmentation phenomena [35], the 2D choice is necessitated by extremely laborious MD computations and justified by a qualitative character of the study. Furthermore, it has been demonstrated not so long ago that *generic* behaviors seem to be shared by fragmenting systems regardless of the *details* of their interaction potentials [8]. Last but not least, the plasticity in confined dimensions is a fascinating and rapidly developing research area in itself (e.g., [36-40]) that is, unfortunately, limited to the quasistatic nanoscale experiments at present; we hope that these simulations are precursors of small-scale dynamic experiments expected in the future.

3 Observations and discussion

The knowledge of the maximum fragment mass dependence upon the impact energy (the initial kinetic energy) of the projectile ($\varkappa \propto v^2$) is of obvious interest for engineering applications. While the mean fragment mass illustrates the average character of the fragmentation process, the maximum fragment mass is potentially of considerable importance for the structural survival analysis since it provides a lower bound for definition of the secondary-impact design events. According to the MD simulation results presented in [28], the scaling relation

$$m_{max} \propto \Xi^{-\xi} \tag{3}$$

captures the elucidated linearity observations within the lower and intermediate part of the hypervelocity impact range, with $\xi \approx 1$ for the generic state variable $\Xi \in \{\varkappa, P_{max}, T_{max}, \dot{\varepsilon}^2_{max}\}$ (Fig. 3). (The variables in braces are the impact energy and the maximum values of pressure, temperature, and strain rate squared, in the order of appearance.) The upper bound for validity of the scaling relation (3) appears to be in the neighborhood of 30 km/s; therefore, Eq. (3) is applicable in the most part of the hypersonic range of practical interest. The dependence of the maximum fragment mass upon the aforementioned state variable Ξ for the *entire* (non-negligible, $\Xi \ge \Xi_0$) fragmentation range is schematically depicted in Fig. 3 by a characteristic reverse-sigmoid curve in the logarithmic space [41].

[3] Note: the rotation of the projectile contour rather than the corresponding lattice itself. Importantly, the projectile lattice configuration with respect to that of the target lattice is not changed.

3.1 Estimation of the shattering transition onset

The terminal or shattering fragmentation (with the onset Ξ_1 or, hereinafter, $\varkappa_1 \propto v_1^2$) is identified in the present study by (the first) occurrence of the uniformly monatomic dust ($m_{max} \equiv 1$) accounting for the deterministic fragment distribution. As already mentioned, the quest for the shattering fragmentation may appear purely academic at present. Be it as it may, estimation of this second critical point ($\varkappa_1$, 1) is pivotal for the completion of the reverse-sigmoid phenomenological model illustrated schematically by Fig. 3.

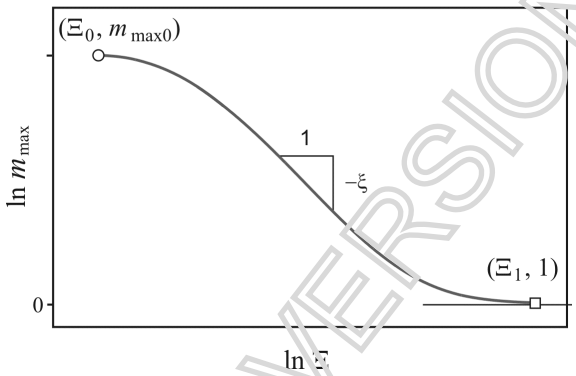

Fig. 3. Schematic plot of the maximum fragment mass vs. the generic state variable $\Xi \in \{\varkappa, P_{max}, T_{max}, \dot{\varepsilon}^2_{max}\}$ in the logarithmic space where the scaling parameter is $\xi \approx 1$ in the approximately linear intermediate hypervelocity range. This model disregards the minuscule fragmentation below the onset of the damage-fragmentation transition, $\Xi < \Xi_0$. (Note that the actual overlap of four reverse-sigmoid curves related to the above-braced variables is achieved by the specific shifts of abscissa values as indicated in [41].)

To facilitate the discussion, the maximum fragment mass vs. the impact velocity in the fragmentation phase ($v \geq v_0$) is presented as a logarithmic plot in the inset of Fig. 4 for three different nanoprojectile sizes, $\bar{d} \in \{19, 33, 53\}$, used in the preceding study [30]. The monotonically decreasing curves exhibit the familiar reversed-sigmoid shape of Fig. 3 with $\xi \approx 2$. Note that only two data points for $\bar{d} = 45$ are marked with symbol "×" in Fig. 4: the critical velocity of the damage-fragmentation transition (known from [30]) and an arbitrarily-selected additional point from the linear range. Similarly to this interpolation, the determination of two (v, m_{max}) data points (for the damage-fragmentation transition and an arbitrarily selected striking velocity in the hypervelocity mid-range) appears sufficient for a reasonably reliable extrapolation of the reverse-sigmoid curves for larger systems that may be too computationally demanding for full-blown computational analyses (e.g., the gray dashed curve on the far right of Fig. 4). Since m_{max} can be considered an order parameter [18], it is reasonable to assume scaling of the $m_{max} = \hat{m}_{max}(v, \bar{d})$ simulation results in well-known form

$$\ln m_{max}(v, \bar{d}) = \bar{d}^{-\beta/\upsilon} F\left\{\left[v(\bar{d}) - v_0(\infty)\right]\bar{d}^{1/\upsilon}\right\} \tag{6}$$

where β is the critical exponent of the order parameter and F designates the scaling function (e.g., [18, 42]) illustrated in the main panel of Fig. 4.

Specifically, the reverse-sigmoid curves in the main panel of Fig. 4 are obtained by rescaling the raw simulation results (shown in the inset of the same figure) by appropriate powers of the nanoprojectile width defined by scaling exponents $\upsilon = 0.77 \pm 0.01$ and $\beta = -0.25 \pm 0.02$. It is important to note that the preceding scaling exponents are identified based on the requirement of the critical-point data (v_0, m_{max0}) collapse [41]. Therefore, unlike the m_{max} vs. v scaling of Timar an co-authors [18] with emphasis on the linear-range data collapse, the main panel plot of Fig. 4 corresponds to the overlap of the first critical points for $\bar{d} \in \{33, 45, 53\}$ (marked by the arrow in the

upper-left corner of Fig. 4). As pointed out in [30], the first critical striking velocity corresponding to $\bar{d} = 19$ is outside the validity range of the scaling

$$v_0(\bar{d}) \propto \bar{d}^{-1/\nu}, \quad \bar{d} \geq \bar{d}_L \approx 23 \tag{7}$$

thus, it is not expected to overlap with other critical points in the main panel of Fig. 4. Eq. (7) manifests the same form of the general size effect well known from the Hall-Petch equation.

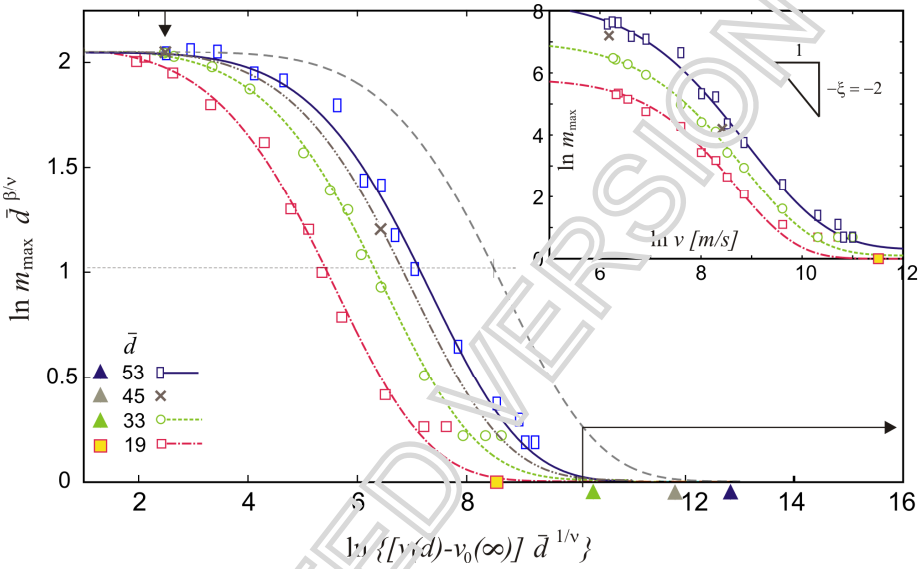

Fig. 4. Inset: Logarithmic plot of the maximum fragment mass (m_{max}) vs. the striking velocity (v) with symbols depicting the MD simulation results for four different projectile widths and curves the corresponding data fits the reverse-sigmoid curves. Main panel: Scaled logarithmic $m_{max} = \hat{m}_{max}(v, \bar{d})$ curves of the inset corresponding to the critical-point (v_0, m_{max0}) collapse for the three different projectile widths $\bar{d} \in \{33, 45, 53\}$ belonging to the power-law (7) validity range [30]. The dashed horizontal in the main panel marks the fifth quantile of dependent variable that corresponds to the inflection point at which the slope is evaluated. The solid square and triangles at the abscissa level designate the shattering fragmentation onsets for the four system sizes as discussed in Section 3.1.

Notably, this effect (summarized in 1950s as "smaller is stronger" and recently endowed with the positively-nuanced meaning "smaller is better" [40]) also exhibits a breakdown at the small end of the system size range that is discussed at length in literature (e.g., [43, 44]). For example, in the recent experimental investigation of plasticity in small-sized metallic systems [36, 38], this saturation plateau of the yield strength is unambiguously observed. Since the onset of the projectile fragmentation, defined by the (first) critical value of the control parameter (e.g., v_0), is inherently related to the material strength, it is physically reasonable that the power law $(7)_1$ should break down at certain point ($\bar{d}_L$), similarly like the strength–vs–size power law observed in the confined-dimensions plasticity. A notable consequence of this breakdown of the power law $(7)_1$ for $\bar{d} = 19$ is that the corresponding critical point is shifted to the left of the overlaping critical points corresponding to $\bar{d} \in \{33, 45, 53\} > \bar{d}_L$, as clearly visible in the upper-left corner of the main panel of Fig. 4.

Importantly, the data presented in Fig. 4 depicts (with the solid square) the occurrence of the shattering fragmentation ($\ln m_{max} \equiv 0$) obtained, not-surprisingly, for the smallest projectile width (diameter), $\bar{d} = 19$, used in the preceding study [30]. The corresponding threshold kinetic energy is

$$\mathcal{K}_1 = \frac{1}{2} M v_1^2 = \frac{1}{2} N_a m_0 v_1^2 \tag{8a}$$

where $M = N_a m_0$ is the total nanoprojectile mass defined in terms of the number of atoms (N_a) and the atomic mass (m_0), while v_1 = 100 km/s is the critical velocity associated with the shattering transition for $\bar{d} = 19$ (Fig. 4).

The energy necessary to rupture all interatomic bonds of the corresponding nanoprojectile (dubbed herein the shattering energy) is

$$\Sigma = N_b \int_{r_0}^{\infty} f(r) dr = N_b \varepsilon \tag{8b}$$

where N_b is the total number of interatomic bonds, f the interatomic force, and ε the strength of attraction (the depth of the potential well) equivalent to the energy necessary to rupture one bond. Based on Eqs. (8), and the data given in Table 2, the ratio of the critical energy and the energy actually needed to rupture all interatomic bonds for $\bar{d} = 19$ nanoprojectile is $(\mathcal{K}/\Sigma)_1$ = 7000. This implies that only 0.014% of the impact energy is actually used for the bond rupture while the rest is transformed into the kinetic energy of the monatomic debris and thermally dissipated during fragmentation process.

The scaled curves in Fig. 4 can be used for estimation of the onset of the shattering transition ($\mathcal{K}_1 \propto v_1^2$) for the larger nanoscale projectiles ($\bar{d} \in \{33, 45, 53\}$). Although it is obvious that this estimate would be more physically sound and likely more realistic than the one based on the linear model, $v_1 \approx 45$ km/s [10], a certain degree of arbitrariness is unavoidable since the reverse-sigmoid curves of Fig. 4 *asymptotically* approach $\ln m_{max} = 0$. Consequently, a criterion is needed to pinpoint the threshold of the elusive shattering transition. The following analysis is performed to address that necessity. It is evident that the normalized critical energy of the shattering fragmentation, $(\mathcal{K}/\Sigma)_1$, must increase with the increase of the nanoprojectile size. The set of additional simulations is performed herein to investigate that size effect. With the notable exception of the smallest nanoprojectile ($\bar{d} = 5$) that deviates towards the small-limit case[4], all other estimates of the shattering transition onset $(\mathcal{K}/\Sigma)_1$ fell rather close to the straight line in the semi-logarithmic space of Fig. 5 regardless of the projectile orientation (Figs. 1a and 1b), the empirical potential, the target density, or the initial temperature of the solid projectile (at least up to T_0 = 1000 K).

Table 2. The critical values of parameters indicating the first appearance of the shattering transition for various nanoprojectile sizes extrapolated (for $\bar{d} > 19$) based on Fig. 5 and scaling relation (9a).

$\bar{d}$ [-]	**19**	**33**	**45**	**53**
N_a	2831	8678	16243	22523
N_b	8150	25435	47910	66606
$(\mathcal{K}/\Sigma)_1$ [-]	7000.	63500.	430000.	$1.50 \cdot 10^6$
v_1 [km/s]	100.	300.	780.	1500.

Based on the trend outlined above, the following scaling relation is proposed

$$\left(\frac{\mathcal{K}}{\Sigma}\right)_1 \propto \exp\left(\frac{\bar{d}}{\delta}\right) \tag{9a}$$

where δ represents the slope in the semi-logarithmic space.

[4] The minimum value of $(\mathcal{K}/\Sigma)_1$ = 14.8 corresponding to v_1 = 268 m/s is obtained for the flat-end impact of the three-atomic system configured as an equilateral triangle.

3.2 Investigation of structural sensitivity of the shattering transition onset

The investigation of structural senstivity of the shattering transition onset values reported herein, is performed by using MD simulations with EAM at T_0 = 1 K with $\bar{d} \in \{9, 13, 17\}$ at two different impact configurations illustrated schematically in Figs. 1a and 1b. The lateral impact test (LIT) results are depicted in Fig. 5 with the laid ellipses (compared to the upright ellipses representing results of the basic slender-projectile rigid-anvil test, that is, the traditional Taylor test (TTT)). Moreover, the simulation corresponding to $\bar{d} = 13$, marked by a dashed vertical line in Fig. 5, in addition to the upright and laid ellipses, depicts a square hollow symbol corresponding to the square-like projectile of the aspect ratio ≈1.0 (Fig. 1c). (Note that all three of these projectiles have the same mass M to within 3%.) The shattering transition onset values, corresponding to this sensitivity analysis, are also reported in Table 3. Each onset value represents the average of five different statistical realizations of the Maxwell-Boltzmann initial velocity field (reflected by the selection of the pseudorandom-number-generator seed). Conspicuously, two bounding impact configurations (TTT vs. LIT) result in the same shattering energy to within 5%. According to Table 3, the shattering transition parameters for the TTT have, consistently, somewhat higher values which is physically sound since the corresponding fragmentation is, compared to the LIT, more non-uniform process[5], characterized, if not precedeed, by a pronounced plastic distortion. This extensive plastic distortion (e.g., the mushrooming evident in Fig. 1) is a disipative process requiring a certain energy.

Table 3. Comparison of two shattering transition parameters obtained by using MD simulations (EAM, T_0 = 1 K) with three different nanoprojectile sizes at two bounding impact configurations: TTT (traditional Taylor test; Fig. 1a) and LIT (lateral impact test; Fig. 1b).

$\bar{d}$ [-]	**9**		**13**		**17**	
	v_1 [km/s]	$\ln(\mathcal{K}/\Sigma)_1$ [-]	v_1 [km/s]	$\ln(\mathcal{K}/\Sigma)_1$ [-]	v_1 [km/s]	$\ln(\mathcal{K}/\Sigma)_1$ [-]
TTT	42.8	7.23	63.6	7.99	80.8	8.46
LIT	42.0	7.12	61.2	7.91	78.8	8.40
Dif. [%]	0.23	1.5	3.8	1.0	2.5	0.71

This data scatter (LIT vs. TTT) is well within the other scattering of the simulation results presented in Fig. 5. (Notably, it is much smaller than the scatter of results among five different statistical realizations of the Maxwell-Boltzmann initial velocity field for the given initial temperature.) This observation suggests that the shattering energy is an inherent, structure-insensitive, property of the material system. If so, the preceding scaling relation (as well as Fig. 5) could be recast in terms of the system mass M:

$$\left(\frac{\mathcal{K}}{\Sigma}\right)_1 \propto \exp\left(\frac{M}{\mu}\right) \tag{9b}$$

The scaling relations (9) are proposed based on the set of MD simulations of the Taylor test with, admittedly, *extremely* small projectiles due to the inherent difficulty, if not inability, to capture the shattering fragmentation with the larger models. It is important to re-emphasize that the system size reduction is instrumental in the effort to achieve the shattering transition – it is a physical necessity rather than an artefact driven by a computational convenience. (There is no the shattering fragmentation at system sizes beyond the certain (rather low) limit!) The scaling relations (9) enable the estimate of the critical energy (or velocity) of the shattering fragmentation ($\mathcal{K}_1 \propto v_1^2$) for the

[5] In general, the more slender the projectile, the more non-uniform the TTT fragmentation process. The thinner the projectile, the more uniform the LIT fragmentation process.

projectile sizes used in the Taylor test simulations (Fig. 4) *under the assumption* that it remains valid for the said range of projectile widths. The extrapolation results are presented in Table 2 and depicted with triangles at the abscissa of the main panel of Fig. 4.

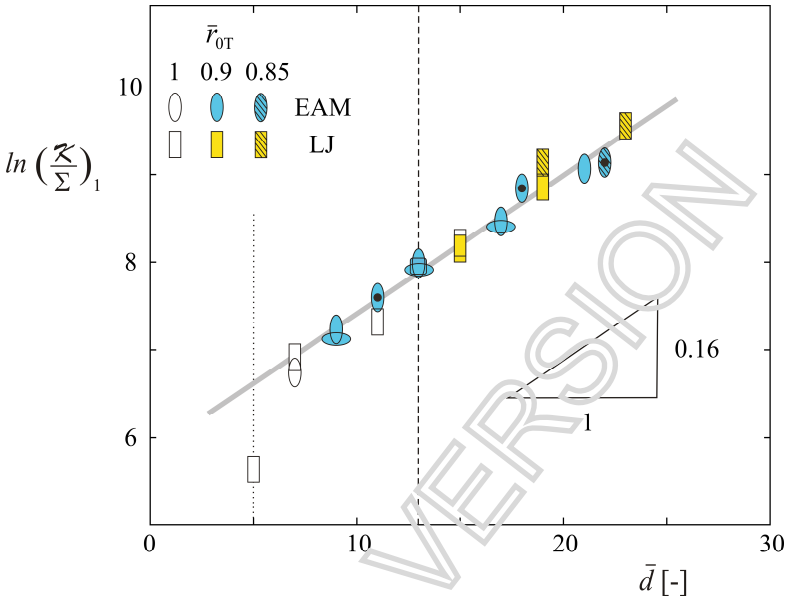

Fig. 5. The normalized energy of the shattering fragmentation plotted for various nanoprojectile sizes. The simulations are performed with LJ potential (rectangular symbols) and EAM method (elliptic symbols) with rigid targets of three different atomic densities (as indicated by the corresponding interatomic distance, $\bar{r}_{0T}$). The EAM simulations are performed at two different temperatures: 1 K and 1000 K; the latter are marked by a solid circle in the middle of the elliptic symbol. Notably, the elliptic data points mark the average value of five different statistical realizations of the Maxwell-Boltzmann initial velocity field (reflected by the selection of the pseudorandom-number-generator seed). The hatched symbols depict three data points obtained for MD simulations with 15% reduction of the target interatomic distance to avoid penetration of the projectile material into the target (i.e. occasional embedding of the projectile atoms into the rigid wall). (The vertical elongation of the upright symbols suggests qualitatively the inherent aleatory variability of the results.)

3.3 Comments on shattering fragmentation onset

Based on the results presented in Table 2, it is obvious why the shattering fragmentation is so elusive for all but the smallest nanoprojectiles. The enormity of the critical velocities shown in Table 2 practically precludes the possibility of successful simulations. More importantly, the physicochemical mechanisms operating at such impact velocities surely exceed the applicability of the traditional MD model. Furthermore, the present simulation results suggest that the shattering transition is not a sharply defined threshold but rather a stochastic property stretched across a relatively wide range of impact energy (which is illustrated purposely by the symbols in Fig. 5 elongated vertically to suggest not only the slender projectiles but also the aleatory variability of the results). Consequently, it seems more reasonable to call it the shattering transition zone rather than the shattering transition onset. Be it as it may, this protracted ("smudged") stochastic approach of the fragmenting system to the shattering transition is rather illustrative of the asymptotic approach it represents in terms of the reverse-sigmoid model represented in Fig. 3.

Finally, the dashed horizontal in the main panel of Fig. 4 designates the fifth quantile of dependent variable $\ln m_{\max}\,\bar{d}^{\,\beta/\nu}$. The corresponding striking velocity, $v_{0.5} = f\left(\bar{d}\right)$, can be used as a location parameter that emphasizes the central tendency for the reverse-sigmoid curve for any given nanoprojectile width. Postprocessing of the simulation results presented in Fig. 4, indicates that $v_{0.5} \propto \exp\left(\bar{d}\right)$ similarly to the expression (9a). Thus, assuming the repeating reverse-sigmoid curves

(as the main panel of Fig. 4), the known estimates of v_0 and $v_{0.5}$ enable positioning of the corresponding reverse-sigmoid curve for an arbitrary projectile size (e.g., the gray dashed curve at Fig. 4), which makes feasible a rough prediction of $m_{\max} = \hat{m}_{\max}\left(\bar{d}, v\right)$.[6] In that way, it is also possible to estimate the minimum achievable $m_{\max}$, for any given projectile diameter, corresponding to some physically-limiting striking velocity $v \le v_{\lim}$. With regards to the results presented in Fig. 4 and Table 2, and bearing in mind the constraint imposed by $v_{\lim}$, it is obvious that for the larger projectiles $m_{\max} >> m_{\max 1} \equiv 1$. Thus, once more, there is a saturation sistem size beyond which the shattering fragmentation is impossible to achieve within the present computational framework.

4 Summary

The simple generic models are used in this study to achieve and investigate, so called, shattering fragmentation defined by the complete (terminal) pulverization of the nanoprojectile into the cloud of monatomic debris ($m_{\max} = m_{\max 1} \equiv 1$). The elusive phenomenon is achieved in the 2D-MD simulations for the very small nanoprojectiles. The results imply that the impact energy significantly exceeds the cohesive energy of the solid sample. In other words, only a miniscule part of the impact energy is actually used for the bond rupture while the overwhelming portion is transformed into the kinetic energy of the monatomic debris and thermally dissipated in the process. An empirical formula is proposed which implies that kinetic energy necessary to achieve the shattering fragmentation depends exponentially on the nanoprojectile width (diameter). This shattering-transition onset (or zone) is seemingly an inherent material property; if so, the preceding empirical formula could be recast in terms of the system mass. Furthermore, this threshold energy appears insensitive either to the choice of the empirical potential or the initial temperature of the solid projectile (at least up to 1000 K). Extrapolation of the proposed phenomenological dependence results in the enormous intensities of the second critical velocity, v_1, that practically preclude the possibility of successful simulations for all but the smallest projectiles. From the standpoint of the fragmentation physics, the striking-velocity limits impose constraints on all but the smallest projectiles that render $m_{\max} >> m_{\max 1} \equiv 1$. Succinctly, the shattering fragmentation is achievable only in the range of very small nanoprojectiles and, consequently, it represents a true asymptote for the fragmentation events at the higher spatial scale.

Acknowledgment

This research was supported by the Ministry of Education, Science and Technological Development of the Republic of Serbia.

References

1. Taylor GI (1948) The use of flat-ended projectiles for determining dynamic yield stress I. Theoretical considerations. Proc Royal Soc Lond A 194 (1038): 289-299.
2. Mastilovic S (2016) Molecular-dynamics simulations of the nanoscale Taylor test under extreme loading conditions. Math Mech Solids 21(3): 326-338.
3. Trunin RF, Medvedev AB, Funtikov AI, et al. (1989) Shock compression of porous iron, copper, and tungsten, and their equation of state in the terapascal pressure range. Soviet Phys. JETP (J. Exp. Theor. Phys.) 68: 356–361.
4. Hixson RS, Fritz JN (1992) Shock compression of tungsten and molybdenum. J Appl Phys 71(4): 1721-1728.

[6] The experimental determination of the first critical point (v_0, $m_{\max 0}$) is a painstaking but a straightforward task. With regards to the current MD simulation framework, a simple estimate of the maximum fragment mass $m_{\max 0}$, is offered in [28] based on geometrical considerations (i.e., the crystallographic orientation of the nanoprojectile of a given size).

5. Grady DE (2006) Fragmentation of Rings Shells. Springer, Berlin Heidelberg New York.

6. Elek P, Jaramaz S (2009) Fragment mass distribution of naturally fragmenting warheads. FME Trans 37: 129.

7. Ramesh KT, Hogan JD, Kimberley J, Stickle A (2015) A review of mechanisms and models for dynamic failure, strength, and fragmentation. Planetary Space Sci 107: 10-23.

8. Sator N, Hietala H (2010) Damage in impact fragmentation. Int J Fract 163: 101.

9. Chen S,Chai H-W, He A-M, Tschentscher T, Cai Y, Luo S-N (2019) Resolving dynamic fragmentation of liquids at the nanoscale with ultrafast small-angle X-ray scattering. J Synchrotron Rad 26: 1-10.

10. Mastilovic S (2015) Impact fragmentation of nanoscale projectiles at ultrahigh striking velocities. Meccanica 50: 2353-2367.

11. Baker KL, Warner DH (2012) Simulating dynamic fragmentation processes with particles and elements. Engng Fract Mech 84: 96-110.

12. Kumar V, Ghosh A (2015) Non-linear dynamic fragmentation using Cracking Particles Method. Comput Mater Sci 98: 117–122.

13. Lai X, Ren B, Fan H, Li S, Wu CT, Regueiro RA, Liu L (2015) Peridynamics simulations of geomaterial fragmentation by impulse loads. Int J Numer Anal Methods Geomech 39: 1304–1330.

14. Rodrigues RS, Birck G, Iturrioz I (2016) Damage index proposals applied to quasi-brittle materials simulated using the lattice discrete element method. Int J Damage Mech 25(7): 1017–1039.

15. Birck G, Antoniox Rinaldi A, Iturrioz I (2019) The fracture process in quasi-brittle materials simulated using a lattice dynamical model. Fatigue Fract Eng Mater Struct: 1–16. https://doi.org/10.1111/ffe.13094.

16. Wittel FK, Carmona HA, Kun F, Herrmann HJ (2008) Mechanisms in impact fragmentation. Int J Fract 154, 105-117.

17. Iturrioz I, Fleck L, Miguel F, Riera JD (2009) Dynamic fracture analysis of concrete or rock plates by means of the Discrete Element Method. Latin Amer J Solids Struct 6: 229 – 245.

18. Timár G, Kun F, Carmona HA, Herrman HJ (2012) Scaling laws for impact fragmentation of spherical solids. Phys Rev E 86(4): 016113.

19. Paluszny A, Tang XH, Zimmerman RW (2014) Fracture and impulse based finite-discrete element modeling of fragmentation. Comput Mech 52(5): 1071-1084.

20. Levy S, Molinari JF (2010) Dynamic fragmentation of ceramics, signature of defect s and scaling of fragment sizes. J Mech Phys Solids 58: 12 –26.

21. Ugrcic M (2013) Numerical simulation of the fragmentation process of high explosive projectiles. Scientific Tech Rev 63(2): 47-57.

22. Paluszny A, Tang XN, Nejati M, Zimmerman RW (2016) A direct fragmentation method with Weibull function distribution of sizes based on finite- and discrete element simulations. Int J Solids Struct 80: 38–51.

23. Wu Y, Wang D, Wu C-T (2014) Three dimensional fragmentation simulation of concrete structures with a nodally regularized meshfree method. Theor Appl Fract Mech 72: 89–99.

24. Li B, Kidane A, Ravichandran G, Ortiz M (2012) Verification and validation of the Optimal Transportation Meshfree (OTM) simulation of terminal ballistics. Int J Impact Engng 42: 25-36.

25. Myagkov NN (2017) Scaling invariance of spherical projectile fragmentation upon high-velocity impact on a thin continuous shield. J Exp Theor Phys 124(1): 57–69.

26. Kun F, Herrmann HJ (1999) Transition from damage to fragmentation in collision of solids. Phys Rev E 59(3): 2623-2632.

27. Redner S (1990 Fragmentation. In: Herrmann H.J., Roux S. (eds): Statistical Models for the Fracture of Disordered. North-Holland, Amsterdam.

28. Mastilovic S (2017) Phenomenology of the maximum fragment mass dependence upon ballistic impact parameters. Latin Amer J Solids Struct 14: 1529-1546.

29. Holian BL, Voter AF, Ravelo RJ (1995) Thermostatted molecular dynamics: How to avoid the Tada demon hidden in Nose-Hoover dynamics. Phys Rev E 52(3): 2338-2347.

30. Mastilovic S (2018) Damage-fragmentation transition: Size effect and scaling behavior for impact fragmentation of slender projectiles. Int J Damage Mech 27(2): 201-217.

31. Holian BL, Voter AF, Wagner NJ et al (1991) Effects of pairwise versus many-body forces on high-stress plastic deformation. Phys Rev A 43(6): 2655-2661.

32. Daw MS, Foiles SM, Baskes MI (1993) The embedded atom method: a review of theory and applications. Mater Sci Reports 9: 251-310.

33. Vrakking MJJ, Lépine F (eds) (2018) Attosecond Molecular Dynamics. RSC Publishing, Cambridge.

34. Diehl A, Carmona HA, Araripe LE et al (2000) Scaling behavior in explosive fragmentation. Phys Rev E 62(4): 4742-4746.

35. Timár G, Blömer J, Kun F, Herrman HJ (2010) New universality class for the fragmentation of plastic materials. Phys Rev Lett 104: 095502.

36. Kraft O, Gruber PA, Monig R, Weygand D (2010) Plasticity in confined dimensions. Ann Rev Mater Research 40: 293-317.

37. Greer JR, De Hosson JThM (2011) Plasticity in small-sized metallic systems: Intrinsic versus extrinsic size effect. Progress Mater Sci 56: 654–724.

38. Rinaldi A (2011) Effects of dislocation density and sample size on plastic yielding at the nanoscale: a Weibull-like framework. Nanoscale 3(1): 4817-4823.

39. Rinaldi A, Peralta P, Sierakowski K et al (2012) Role of dislocation density on the sample-size effect in nanoscale plastic yielding. J Nanomech Micromech 2(3): 42-48.

40. Rinaldi A, Aranco A, Velozzi S et al (2014) The clash of mechanical and electrical size-effects in ZnO nanowires and a double power law approach to elastic strain engineering of piezoelectric and piezotronic devices. Adv Mater 26(34): 5976-5985.

41. Mastilovic S (2018) Some sigmoid and reverse-sigmoid response patterns emerging from high-power loading of solids. Theor Appl Mech 45(1): 95-119.

42. Stauffer D, Aharoni A (1992) Introduction to Percolation Theory. Taylor & Francis, London.

43. Zhu T, Li J, Samanta A et al (2008) A temperature and strain-rate dependence of surface dislocation nucleation. Phys Rev Lett 100: 025502.

44. Li Q-J, Ma E (2018) When 'smaller is stronger' no longer holds. Mater Res Lett 6(5): 283-292.

45. Holian BL, Grady DE (1988) Fragmentation by molecular dynamics: the microscopic "big bang". Phys Rev Lett 60: 1355-1358.